Implosion and Burn of Fast Ignition Capsules - Calculations wioth HYDRA

H. D. Shay, P. Amendt, D. Clark, D. Ho, M. Key, J. Koning, M. Marinak, D. Strozzi, M. Tabak

April 19, 2012

Disclaimer

This document was prepared as an account of work sponsored by an agency of the United States government. Neither the United States government nor Lawrence Livermore National Security, LLC, nor any of their employees makes any warranty, expressed or implied, or assumes any legal liability or responsibility for the accuracy, completeness, or usefulness of any information, apparatus, product, or process disclosed, or represents that its use would not infringe privately owned rights. Reference herein to any specific commercial product, process, or service by trade name, trademark, manufacturer, or otherwise does not necessarily constitute or imply its endorsement, recommendation, or favoring by the United States government or Lawrence Livermore National Security, LLC. The views and opinions of authors expressed herein do not necessarily state or reflect those of the United States government or Lawrence Livermore National Security, LLC, and shall not be used for advertising or product endorsement purposes.

Implosion and Burn of Fast Ignition Capsules – Calculations with HYDRA

H. D. Shay, P. Amendt, D. Clark, D. Ho, M. Key, J. Koning, M. Marinak, D. Strozzi, and M. Tabak

Lawrence Livermore National Laboratory, Livermore, California 94551

We present a methodology for conducting the design calculations for Fast Ignition indirect-drive implosions with an embedded cone for introducing a second laser beam to ignite the compressed fuel. These calculations are tuned to achieve to achieve several design goals. We demonstrate a major feature of the implosion simulations, the lagging of the implosions along the cone. Possible avenues for enhancing the coupling of the fast electrons to the dense compressed DT fuel are discussed.

I. Introduction

An alternative to inertial fusion with isobaric central hot-spot ignition is "fast ignition" (FI), in which one laser compresses the DT fuel and a second laser with a short, very intense pulse heats a small region in the compressed fuel with super-thermal electrons[1], causing isochoric ignition. The potential advantage of fast ignition is that it can achieve the higher gain because isochoric ignition requires less dense fuel with less energy invested in compression and less severe convergence and stability concerns. The relativistic electrons generated by the high-intensity, short-pulse ignitor beam have a broad angular distribution[2], and this has motivated the use of a hollow reentrant cone to provide a path for the laser to be focused close to the compressed fuel. Experimental study of fast ignition has used cone coupling in targets that are an order of magnitude smaller in scale than is required for high gain, about 100, of interest, for example, for inertial fusion energy (IFE). This paper explores the design of targets for high gain using numerical modeling.

Several important design issues arise in cone coupled FI including: (1) asymmetry of implosion, (2) cone metal impurity mixing with the DT fuel, (3) spall from shocking the inner surface of the cone and subsequently occluding the ignitor beam, (4) the tip of the cone being crushed and/or penetrated by the high pressures generated in the compressed DT core, (5) the site of the ignitor laser absorption too far from the region of high density DT, and (6) the areal density of the compressed cone tip being too great for penetration by the fast electrons. This study seeks designs that successfully address these problems.

We have used the 2D-3D HYDRA radiation-fluid dynamics code[3] to conduct calculations of implosions and subsequent thermonuclear burn. We have studied two different scales of design:

(1) one suitable for an IFE power plant.

(2) one testing the concept using the National Ignition Facility[4].

Experiments[5] and simulations[6] have both indicated that the MeV electrons produced by the absorption of intense laser beams are sprayed into very wide angles. Consequently, we have examined implosions that would be conducive to guiding these electrons toward the high density DT by the use of self-generated or compressed magnetic fields.

This paper treats the indirect-drive implosion of capsules in the reentrant cone geometry. A subsequent paper will examine simulations of the heating of imploded configurations by MeV electrons generated by intense laser beams focused on the interior of the cone tip. The simulations reported here use indirect drive and follow the design methodology with the radiation-hydrodynamic codes (LASNEX and HYDRA) from the National Ignition Campaign. Two approaches to fuel compression have been developed: a four shock capsule[7] used for the IFE scale design and a one shock capsule[8] for the NIF scale design.

II. 1D capsule designs

In the current article, we have started with a 1D LASNEX calculation of a hohlraum with close approximation at the physical dimensions of the capsules and with an artificial "leakage hole" to mock up radiant losses through the laser entrance holes. This simulation defines a frequency dependent source (FDS, a function of time) from the laser interaction in the hohlraum. The FDS is then applied to drive subsequent 1D LASNEX[9] implosions of the capsule, and the pulse shape is tuned to optimize the implosion. An optimal tune maximizes high density and ρR in the imploded DT configuration. The LASNEX based 1D tuned capsules are used as the starting point for the 2D HYDRA modeling.

Figure 1 depicts the pie diagrams for the "reactor scale" and "NIF scale" capsules. In both cases, the beryllium ablator has an internal layer doped with Cu. These layers are to prevent preheating of the ablator/DT ice interface and the gold cone by gold M-band radiation generated in portions of the hohlraum wall directly heated by laser beams. To achieve greater ablation pressure the outer layer of beryllium is not doped. A thin layer of undoped beryllium lines the inside of the ablator so that there less heating and decompression at the Be/DT interface to achieve a lower Rayleigh-Taylor instability Atwood number. The mass of the DT fuel is 3mg for the "reactor scale" capsule and 0.59mg for the "NIF scale" capsule

Figure 2 show the respective equivalent radiation temperatures of the two FDS's - the red curve for the NIF scale capsule and the black curve for the reactor scale capsule. The energy absorbed by the capsules is about 580kJ and 150kJ, respectively, which implies, for expected hohlraum coupling efficiencies of 25-33%[4], laser energies (implosion drive only) of about 1.7-2.3MJ and 0.45-0.60MJ. The 1D HYDRA calculations that the times of peak densities of 230 and 200g/cc, respectively, occur at 56.2 and 32.5ns and have values of peak DT ρR of 2.8 and 2.0g/cm^2. The 1D yield of the reactor scale capsule is 277MJ for a gain (counting implosion laser energy only) of about 120 to 160.

III 2D HYDRA Implosions – methodology

In the 2D HYDRA simulations we have explored a number of design parameters, defined in figure 3a and 3b. The cone is characterized by inner and outer angles, θ_{in} and θ_{out}, and the outer surface of the cone may point off the center of the capsule by δ_{point}. The nose of the cone has a wall thickness on axis of δ_{wall} and the tip of the nose is offset from the center of the capsule by δ_{offset}. Typically our calculations have set θ_x to zero so that the cone outside of the capsule shell is a cylinder with its wall parallel with the axis of the cone. Additionally, we have in a few cases examined the effect of imposing a perturbation of $\delta P1(\cos\theta)$ to the radii of all the shells such that the radii are reduced at the cone side of the implosion. We have also considered Legendre perturbations to the symmetry of the frequency dependent source so that the drive is enhanced at the cone side. Figure 3b shows a cone nose which is the same metal as the cone itself, gold, but we have also examined cases for noses of copper or diamond (carbon at density 3.51g/cc), the latter as depicted in figure 4.

To provide greater facility in allocating zones, HYDRA permits the calculation to be broken up into "user blocks" with the grid defined in each with the sole criterion that the nodes on the boundary of one block must correspond to the nodes of the adjacent block. Figure 5 shows a typical "user block" decomposition and the associated meshes. Note that at the node at the corner of a block may have either standard connectivity (in 2D, each node is connected to four other nodes) or reduced connectivity (in 2D, a node connected to just three other nodes). The outer surface of the capsule ablator typically has zones initially of 1μm thickness, with zones increasing in thickness toward the interior. The inner surface of the DT ice initially has zones about ½ μm in thickness. The angular resolution in zoning is 1° for most of the capsule and is finer near the cone.

The hydrodynamics in HYDRA is ALE, Arbitrary Lagrangian Eulerian. Typically, most of the capsules shell (except of the portion adjacent to the cone) is left purely Lagrangian (without the relaxation and Eulerian phases) until the first shock breaks out of the DT ice layer. Additionally, in areas subject to severe mesh distortions, periodic remapping of the mesh is invoked.

These calculations have used QEOS[10] for the equations of state of all the materials. The QEOS model uses a combined analytic/Thomas-Fermi EOS with a modified Cowan model for the ion EOS and with a scaled Thomas-Fermi table for the electron EOS. One great advantage of using QEOS instead of tabular equations of state, which may be based on more sophisticated theories, is that, in extracting values from tables, numerical noise may be generated that engenders destructive fluid instabilities. Because of the high pressures and temperatures, we have not used any constitutive models to represent strength of materials.

Because the ablated surface of the gold cone presents a plume which can shadow a portion of the capsule from the FDS (for example, see figure 6), we have chosen to use implicit Monte Carlo (IMC) x-ray transport. Frequency dependent opacities using average atom approximation in local thermodynamic equilibrium have been used for transporting the Monte Carlo photons.

For simulations with imposed axial magnetic fields, we have used the MHD package in HYDRA that implements the resistive magnetohydrodynamics equations using the formulation based on the finite element method of Bochev, Hu, Robinson, and Tuminaro[11]. This method has been augmented with an optional source terms for Ohm's law as well as a potential gradient term. The advection method is a constrained transport method limiting the magnetic fluxes through a divergence conserving edge voltage limiter.

IV Implosion Results

In performing these simulations, we have tuned the geometry of the cone, the P1 radial variations of the capsule, and the angular variation of the x-radiation source, but have not altered the 1D geometry of each of the two designs. This tuning has been conducted to satisfy a number of criteria, some of which are summarized in figure 7. Of paramount importance is for the implosion to attain a density of DT greater than 200g/cc and a value of ρR greater than 2g/cm^2 since Atzeni[12] demonstrated that the energy required in the ignition zone varies as $\rho^{-1.85}$ and since Nuckolls[13] showed that the fraction of DT fuel consumed by thermonuclear burn is $\rho R/(\rho R + 6g/cm^2)$. Because the MeV electrons are generated with a very broad angular distribution, it is important for the distances X and Y to be a short as possible. Likewise, to minimize the energy loss of the electrons in traversing matter between the laser interaction surface and the high density DT the integrals of ρds along those paths must be small not to degrade the coupling to the ignition zone. For example, for a 3 to 20 MeV electron, the stopping power is about 1.5 MeV/(g/cm^2), approximately independent of material. In as much as the elastic scattering cross-section varies roughly as Z, to avoid even greater angular dispersion of the electron beam and concomitant path lengthening, low Z materials seem preferable for the "nose" of the cone. The electron energy spectra, depending on the laser intensity[14], can easily extend up to 10 MeV and, since the bremsstrahlung cross-section varies roughly as Z^2 and increases rapidly with electron energy, the reduction of radiative losses also argue in favor of low Z noses. To present an unperturbed surface to the ingitor laser beam and to prevent occluding of its path inside the cone, we have also paid attention to the timing of the shock break-out on the interior of the cone, which is thinnest near the transition to the "nose" and on the surface of the "nose." As illustrated for the design in figure 7, the shock has not yet emerged from the cone and has just broken out of the "nose"

3

on axis at the time of peak DT density. This consideration emphasizes the use of high density material for both cone and nose just to present greater inertia in the smallest volume. Since there are no concerns about areal density being too great across any part of the cone other than the "nose", gold is used there, but, because of the countervailing arguments in favor of low areal density and low Z for the nose a variety of materials of the "nose" have been used there. Various sandwiches of materials have also been explored in order to get the appropriate gradients in resistivity to the thermal electron return current that have been predicted by Robinson[15] to provide large confining magnetic fields.

In the course of the implosion, the side of the capsule shells nearest the cone lags behind the other side, as illustrated in the NIF-scale implosion shown in figures 8 and 9. This lagging arises from two effects. The gold cylinder leading to the cone ablates into the hohlraum volume and thus shadows the surface of the capsule from the x-ray source, as shown in figure 6. We thus find that the radiation energy density is lower at the ablation surface of capsule near the cone than elsewhere on the capsule ablation surface. A second effect is that the capsule ablation surface launches a shock tangentially into the cone, thereby permitting the ablation pressure there to fall, while at other points on the capsule ablation surface far from the cone no such tangential relaxation is possible. Because of the lagging of the implosion along the cone, some fraction of the DT is left behind along the surface of the cone. Figure 9 shows that the velocity of the captured DT is far below the implosion velocity. Consequently, any gold ablated off of the cone or entrained by Richtmyer-Meshkov fluid instabilities is not transported down to the center of convergence. The only danger of mixing of the cone material with the high density, imploded DT seems to arise near the tip of the cone. The use of other materials, such as diamond, near the tip of the cone has been explored. Alternatively, we have found that a relatively thin layer of beryllium or diamond, less than $10\mu m$ thickness, can suppress gold ablation even at the tip.

The simple definition of the DT ρR suggested by the arrow in figure 7 is illusory in that implosion asymmetries cause the burn-up fraction to be lower than that implied by this measure of ρR. A useful measure represents some average ρR. One easily defined average ρR is to fit a spherical surface to the right-hand-side of the implosion, which is fairly symmetric, determine the DT mass within that sphere, and, assuming average density, calculate the equivalent average areal density ρR, as indicated in figure 10. This measure represents a lower bound on the average areal density because of the use of constant DT density. By the measure of figure 7, the DT ρR is $2.39 g/cm^2$, not too far below the 1D value for that capsule, but by the average ρR derived by this alternated procedure is $1.33 g/cm^2$. In typical cases in which the imploded DT is ignited by the ad-hoc heating of a small patch, the resulting burn-up fraction lies between the max ρR and this average ρR. For example, a reactor scale implosion with a diamond nose has a ρR of $2.5 g/cm2$ and an average ρR of $1.4 g/cm2$; its yield is 216MJ, a burn-up fraction of about 22% and the theoretical burn-up fraction is about 19% based on the average ρR.

Both the peak DT density and average ρR in our 2D calculations are less than the results obtained in the corresponding 1D calculations. For the NIF scale capsule, the best values attained in 2D simulations are average ρR of about $0.8 \ g/cm^2$ in contrast to the 1D values of about $2.1 \ g/cm^2$. For the reactor scale capsule, the 2D simulations attain average ρR of about $1.4-1.7 \ g/cm^2$ and maximum ρR of about $2.5 g/cm^2$, while the 1D values are about $2.8 g/cm^2$.

Much of the tuning of the cone has focused on reduced the distances across the nose and to the peak DT density, X and Y, and the areal densities across those distances. Table 1 illustrates the results of one series of reactor scale simulations that employed a diamond nose. In these calculations, the peak DT density typically ranges from 230g/cc to 260g/cc and the average ρR about $1.4 g/cm^2$. In all of these

simulations, the gold cone ends and diamond nose begins at a radius of 100μm; on the axis, the vacuum side of the nose is located at 140μm from the origin while the distance from the origin on the DT side is designated as the "tip of the nose" (δ_{offset} in figure 3b), minus for noses ending to the left of the origin and positive for those protruding beyond the origin. Most of the tips of the noses are protruding cylinders with a radius of 50μm. These have no extra notation in the "tip of the nose" column, but the last, D2EK, has a radius of 100μm and the second, third, and fourth, D2EA, D2EB, and D2EC, are tapered to zero radius on the axis (noted as "sloped"). The second column denotes the P1 offset to the ablator and DT ice shells. All of these simulations have cones with an inner angle of 34°, and the projected offset of the cone ($\delta_{pointing}$ in figure 4) ranges from 0 to 75μm. Since the nose is deformed at the time of peak DT density, the values of X and Y and the corresponding areal densities are sometimes shown as ranges. Generally speaking, the total distance from the surface where the fast electrons are generated to the region of peak DT density is roughly 100-200μm, and the net areal densities along that path, about 1.5-2.0g/cm². Without some means of focusing and/or guiding the electrons, perhaps by magnetic fields, these distances would result in a small fraction of the ignitor laser energy being deposited in the high density DT.

V Burn calculations

Under what circumstances would these imploded 2D configurations ignite and to what efficiency would they burn? Before addressing the issue of self-consistently heating the DT with a spectrum of fast electrons generated by an intense laser beam inside, the energy required to heat the compressed DT to ignition was determined as follows. A dump from a calculation at the time of peak DT density was mapped onto a very finely zoned Cartesian mesh. A fraction of the DT around the site of peak density was heated with a constant power over several picoseconds. Figure 11 shows one of the burn calculations for a reactor scale capsule at the beginning of the heating pulse that is delivered to a mass of DT between the 200 and 250g/cc density contours. The several burn calculations based on this implosion all had this Cartesian grid with a spacing of 1μm and used Eulerian advection without any mesh motion. In the several burn calculations based on the same implosion, the energy was injected into the electrons of two different DT masses, 20 and 65μg, which had average ρR of approximately 0.32 and 0.50g/cm2. Figure 12 displays the yield as a function of the programmed energy for a heating duration of 10ps. The sequence with 65 μg indicates that ignition will occur for ion temperatures above 9keV. The threshold for ignition given by Atzeni's relationship[16]

$$E = 140kJ \left(\frac{\rho}{100g/cc} \right)^{-1.89}$$ (1)

is about 24-27kJ. While the energy required for ignition may only be about 30kJ, depending on the angular and energy distributions of the fast electrons, without focusing of the electrons, several mega-joules of laser energy may be needed.[17] We have consequently investigated techniques with magnetic fields for focusing or guiding the fast electrons from the region of laser deposition to the region of high density DT.

VI Designs for magnetic guiding or focusing

We have begun study of two schemes for using strong magnetic fields. The first is to impose an axial magnetic field before the beginning of the implosion and then to compress it during the implosion, a

technique that has been demonstrated in experiments at the U. of Rochester.[18] A series of simulations has been conducted for NIF scale implosion with a uniform axial field of 100kG. Electrical conductivity has been modeled by the Purgatorio[19] code for all materials with the exception of the gold cone, for which conductivities were predicted by the model of Lee-More-Desjarlais[20]. These simulations demonstrate very large magnetic fields in the compressed DT, more than 150MG. Since the gyroradius of a 5 MeV electron in a 100MG field is less than 2μm, these fields are strong enough to guide the fast electrons from the region of laser absorption to the high density DT.

This technique has several possible difficulties. A major problem is that as the fast electrons are being guided along lines of magnetic field, they are encountering an increasing field strength and, consequently, may be reflected back in the opposite direction by the mirror effect. As shown by Strozzi[21], for the anticipated angular distribution of electrons, a sharp rise of a factor of two in magnetic field results in an increase in the fraction of electrons reflected by about a factor of three. The HYDRA implosion simulations of the NIF scale capsule show that the magnetic field diffuses poorly through the gold cone. At 32ns, the field in the region of laser absorption is less than 10MG while in the compressed DT, less than 400μm away, the field may be as large as 155MG, a result that would be highly susceptible to magnetic mirroring. The result depends, among other factors, on the rate at which the magnetic field diffuses into the gold cone, a rate governed mainly by the conductivity of gold as it is being heated and making the transition from a metal with conduction bands to a plasma. In this regime there may be large uncertainties in the conductivity. With nominal gold conductivity, the field at the laser deposition site is less than 10MG, and even with the gold conductivity reduced arbitrarily by a factor of 10^4, the field at that site is still less than 10MG. Exploration of these designs will probably require a high density, insulating cone.

The second approach is to use the magnetic fields generated by gradients in resistivity, as noted in the paper by Robinson[14], where the term giving rise to the azimuthal field is

$$\frac{\partial B}{\partial t} = \nabla \eta \times J_f + \eta \nabla \times J_f \qquad (2)$$

where J_f is the current of fast electrons. For the magnetic field to have the correct sign to bend the fast electrons back toward the axis, the gradient in resistivity should be oriented such that the higher resistance material is at smaller radius than the lower resistance material. Since, for equal density and temperature, higher Z material will have a greater resistance than lower Z material, appropriate designs should have higher Z material nearer the axis, for example, a nose of gold overlaid with a layer of copper. Hybrid calculations with MC electrons (to be discussed in a subsequent paper) indicate that this configuration would indeed have large magnetic fields of the proper sign, but the areal density in the gold is too large, between 1.5 and 3.8g/cm^2, depending on the path, and only a small fraction of the fast electron energy would be deposited in the dense DT. Alternatively, one may have a nose that protrudes into the DT; hybrid calculations with a diamond nose indicate that there too magnetic fields of tens of mega-Gauss would be generated.

VII Conclusions

We have explored a portion of the design space for Fast Ignition implosions with a wide variety of cone shapes and materials for two different capsule sizes. We have demonstrated that, while the asymmetry of the implosion can degrade the peak DT density and ρR, there are designs that do approach 1D parameters and give reasonably efficient DT burn if ignited with sufficient energy deposited in the high density DT. Because of the lagging of the implosion adjacent to the cone surface, the chance of cone

material being swept down to the center of convergence is very much reduced. The issue of transporting a large fraction of the fast electrons from the laser interaction region to the high density DT remains a difficult problem, which will be addressed in a future paper using integrated calculations of the hybrid of the PIC code ZUMA and the radiation-hydrodynamics code HYDRA.

ACKNOWLEDGEMENTS

FIGURE CAPTIONS:

Fig. 1. 1D designs used in 2D study; (a) for NIF scale experiment; (b) for a power reactor scale capsule.

Fig. 2. These curves are the equivalent radiation temperature for the frequency dependent source. The red curve characterizes the NIF scale capsule; the black curve, the reactor scale capsule.

Fig. 3. These are definitions of the geometrical design parameters. (a) θ_{in} and θ_{out} are the inner and outer slopes of the cone. θ_{rad} is the angular variation of the frequency dependent source; (b) δ_{wall} is the thickness of the nose on axis; δ_{offset} is the distance from the nose to the center; $\delta_{pointing}$ represents a shift in the centering of the cone.

Fig. 4. This figure illustrates the use of a diamond nose instead of gold. Here the interface of the diamond slopes directly to the axis, but in some designs, we have simulated geometries in which there is a cylindrical projection protruding into the DT.

Fig. 5. These figures show a typical blocking structure for these HYDRA simulations. (a) The colored regions show different blocks, each with their own indices for the mesh nodes. The dark lines are the interfaces between the several material regions. (b) This is an enlargement of the central portion of the mesh with one of the points of reduced connectivity highlighted. (c) This enlargement shows the mesh lines. The central block (#0, red) has a very high density of mesh lines because of the convergence of the mesh lines from all the other blocks. This scheme provides high resolution at the center of convergence, but avoids mesh convergence to a point, a scheme that would have resulted in extremely small Courant time steps.

Fig. 6. This illustration shows a simulation of a reactor scale capsule in the middle of its implosion, at 30ns. The pseudo-color plot represents the equivalent radiation temperature for the multi-group radiation energy density. The dark lines are the material boundaries. The faint lines in the DT indicate the trajectories of the very few IMC particles that have leaked through the doped ablator.

Fig. 7. This figure shows an imploded capsule at the time of peak density in the DT, with the pseudo-color indicating $\log(\rho)$ and contour for 100 and 250g/cc in the DT. Several key parameters are shown. So that the vacuum path on the interior of the cone is not occluded, we endeavor to tune the design so that shocks do not break out of the interior surface before the ignitor beam starts. We try to minimize the path

lengths (X and Y) and areal densities through the nose and from the nose to the locus of the peak DT density. Better designs have larger peak DT density and DT ρR, here just suggested by a single path integral through the peak DT density.

Fig. 8. This sequence of images displays the implosion of a NIF scale capsule, from the middle of the implosion at 24ns to the time of peak DT density at 32.5ns. Note that the scales change as the implosion progresses. At 32.5ns, the pressure in the compressed DT has ruptured the nose of the cone, signifying a faulty design.

Fig. 9. This illustration is taken from the implosion of a NIF scale capsule at 31.5ns, within about 1ns of the peak DT density. It highlights the behavior of the DT and ablator near the cone. The pseudo-color indicates speed and the arrows, velocity. As a shock is launched into the gold cone, visible as the lighter blue, the implosion along the cone is retarded. Some DT is captured between the ablator and the cone with a much lower velocity than the rest of the imploding DT. These simulations thus suggest that along most of the cone, there is little entrainment of cone material into the imploding DT.

Fig. 10. This figure illustrates a crude procedure for obtaining an average ρR for the imploded DT. A sphere is fitted to the right-hand-side of the DT/ablator interface, here a sphere of radius, R, 193mm centered at 40mm. Inside that sphere the log of the DT density is depicted by pseudo-color. The average density within the sphere is determined, $<\rho>$, and the average ρR is estimated as $<\rho>R$.

Fig. 11. This figure shows the region heated in a burn study. The black lines are the region interfaces and the colored lines, DT density contours, from 50 to 250g/cc. The red patch indicates where the energy is sourced into the electrons.

Fig. 12. This graph shows the results of the burn studies for the implosion of one reactor scale design. The abscissa, E_{in}, is the total energy programmed into the region depicted in red in Fig. 11 over a duration of 10ps, and the ordinate, the thermonuclear yield. The blue curve has a DT mass of 20μg in the heated region; the red curve, 65μg.

Table 1. This table shows the results of some of the implosion simulations conducted with reactor scale designs having diamond noses, carbon of initial density 3.51g/cc. The column labeled tip of nose displays the axial position of the nose relative to the origin, sometimes with notations indicating the variations in the shape of the nose. The P1 column shows the P1 shift of the shells. The offset column shows the position of the projection of the outer surface of the cone to the axis. These input design parameters are all summarized on the diagram in figures 3a and 3b. The results are the shown in the columns X, IX, Y, and IY, the definitions of which are summarized in figure 7.

[1] M. Tabak, J. Hammer, M. E. Glinsky, W. L. Kreur, S. C. Wilks, J. Woodworth, E. M. Campbell, M. D. Perry, and R. J. Mason, Phys. Plasmas **1**, 1626 (1994).

[2] R. B. Stephens, R. A. Snavely, Y. Aglitskiy, F. Amiranoff, C. Andersen, D. Batani, S. D. Baton, T. Cowan, R. R. Freeman, T. Hall, S. P. Hatchett, J. M. Hill, M. H. Key, J. A. King, J. A. Koch, M. Koenig, A. J. MacKinnon, K. L. Lancaster, E. Martinolli, P. Norreys, E. Perelli-Cippo, M. Rabec Le Gloahec, C. Rousseaux, J. J. Santos, and F. Scianitti., Phys. Rev E **69**, 066414 (2004).

Y. Sentoku, H. Ruhl, K. Mima, R. Kodama, K. A. Tanaka, and Y. Kishimoto., Phys. Plasmas **6**, 2855 (1999).

J. S. Green, V. M. Ovchinnikov, R. G. Evans, K. U. Akli, H. Azechi, F. N. Beg, C. Bellei, R. R. Freeman, H. Habara, R. Heathcote, M. H. Key, J. A. King, K. L. Lancaster, N. C. Lopes, T. Ma, A. J. MacKinnon, K. Markey, A. McPhee, Z. Najmudin, P. Nilson, R. Onofrei, R. Stephens, K. Takeda, K. A. Tanaka, W. Theobald, T. Tanimoto, J. Waugh, L. VanWoerkom, N. C. Woolsey, M. Zepf, J. R. Davies, and P. A. Norreys, Phys. Rev. Letters **100**, 015003 (2008).

K. Lancaster, J. S. Green, D. S. Hey, K. U. Akli, J. R. Davies, R. J. Clarke, R. R. Freeman, H. Habara, M. H. Key, R. Kodama, K. Krushelnick, C. D. Murphy, M. Nakatsutsumi, P. Simpson, R. Stephens, C. Stoeckl, T. Yabuuchi, M. Zepf, and P. A. Norreys., Phys. Rev. Letters **98**, 125002 (2007).

[3] M.M. Marinak, G. D. Kerbel, N. A. Gentile, O. Jones, D. Munro, S. Pollaine, T. R. Dittrich, and S. Haan , Phys. Plasmas **8** , 2275 (2001).

[4] J. D. Lindl, Inertial Confinement Fusion, Springer-Verlag, New York (1998).

[5] M. H. Key, M. D. Cable, T. E. Cowan, K. G. Estabrook, B. A. Hammel, S. P. Hatchett, E. A. Henry, D. E. Hinkel, J. D. Kilkenny, J. A. Koch, W. L. Kruer, A. B. Langdon, B. F. Lasinski, R. W. Lee, B. J. MacGowan, A. MacKinnon, J. D. Moody, M. J. Moran, A. A. Offenberger, D. M. Pennington, M. D. Perry, T. J. Phillips, T. C. Sangster, M. S. Singh, M. A. Stoyer, M. Tabak, G. L. Tietbohl, M. Tsukamoto, K. Wharton, and S. C. Wilks, Phys. Plasmas **5**, 1966 (1998).

[6] A. J. Kemp and L. Divol, submitted to Physical Review Letters (2011).

[7] S. Haan, J. D. Lindl, D. A. Callahan, D. S. Clark, J. D. Salmonson, B. A. Hammel, L. J. Atherton, R. C. Cook, M. J. Edwards, S. Glenzer, A. V. Hamza, S. P. Hatchett, M. C. Hermann, D. E. Hinkel, D. D. Ho, H. Huang, O. S. Jones, J. Kline, G. Kyrala, O. L. Landen, B. J. MacGowan, M. M. Marinak, D. D. Meyerhofer, J. L. Milovich, K. A. Moreno, E. I. Moses, D. H. Munro, A. Nikroo, R. E. Olson, K. Peterson, S. M. Pollaine, J. E. Ralph, H. F. Robey, B. K. Spears, P. T. Springer, L. J. Suter, C. A. Thomas, R. P. Town, R. Vesey, S. V. Weber, H. L. Wilkens, and D. C. Wilson., Phys. Plasmas **18**, 051001 (2011). This reference has a discussion of a similar design philosophy.

[8] D. S. Clark and M. Tabak, Nuclear Fusion **47**, 1147 (2007).

[9] G. Zimmerman and W. Kreur, Comments on Plasma and Controlled Fusion **2**, 51 (1975).

[10] R. M. More, K.H. Warren, D.A. Young, G.B. Zimmerman, Phys. Fluids **31**, 3059 (1988).

[11] P. B. Bochev, J. J. Hu, A. C. Robinson, and R. S. Tuminaro, "Toward Robust 3D Z-pinch Simulations: Discretization and Fast Solvers for Magnetic Diffusion in Heterogeneous Conductors," Electronic Transactions on Numerical Analysis **15**, 186 (2003).

[12] S. Atzeni, Physics of Plasmas, **6**, 3316 (1999).

[13] J. H. Nuckolls, "*Laser-induced implosion and thermonuclear burn*," Laser Interaction and Related Plasma Phenomena, edited by H. J. Schwartz and H. Hora, **3B**, 399 (1994).

[14] Strozzi, M. Tabak, D. J. Larson, M. M. Marinak, M. H. Key, L. Divol, A. J. Kemp, C. Bellei, and H. D. Shay, "Cone-Guided Fast Ignition with no Imposed Magnetic Fields," Proceedings of IFSA Conference (2011), to be published.

[15] A. P. L. Robinson, M. Sherlock, Phys. Plasmas **14**, 083105 (2007).

[16] Stefano Atzeni, Angelo Schiavii, and Claudio Bellei, Phys. Plasmas **14**, 052702 (2007).

[17] D. J. Strozzi, M. Tabak, D. J. Larson, L. Divol, A. J. Kemp, C. Bellei, M. M. Marinak, and M. H. Key, "Fast-ignition design transport studies: realistic electron sources, integrated PIC-hydrodynamics, imposed magnetic fields," to be published in Physics of Plasmas.

[18] O.V. Gotchev, P. Y. Chang, J. P. Knauer, D. D. Meyerhofer, O. Polomarov, J. Frenje, C. K. Li, M. J.-E. Manuel, R. D. Petrasso, J. R. Rygg, F. H. Séguin, and R. Betti., Phys. Rev. Letters **103**, 215004 (2009).

J.P.Knauer, O. V. Gotchev, P. Y. Chang, D. D. Meyerhofer, O. Polomarov, R. Betti, J. A. Frenje, C. K. Li, M. J.-E. Manuel, R. D. Petrasso, J. R. Rygg, and F. H. Seguin., Phys. Plasmas **17**, 056318 (2010).

[19] S. B. Hansen, W. A. Isaacs, P. A. Sterne, B. G. Wilson, V. Sonnad, and D. A. Young., "Electrical Conductivity from the Purgatorio Code," Proceedings of the 2005 NEDPC, UCRL-PROC-218150 (2006).

[20] Y. T. Lee and R. M. More, Physics of Fluids **27**, 1273 (1984).

M. P. Desjarlais, Contrib. Plasma Physics **41**, 267 (2001).

[21] D. J. Strozzi, "Cone-Guided Fast Ignition with Imposed Magnetic Fields," 7th International Conference on Inertial Fusion Science and Applications, Bordeaux, France, September 12-16, 2011.
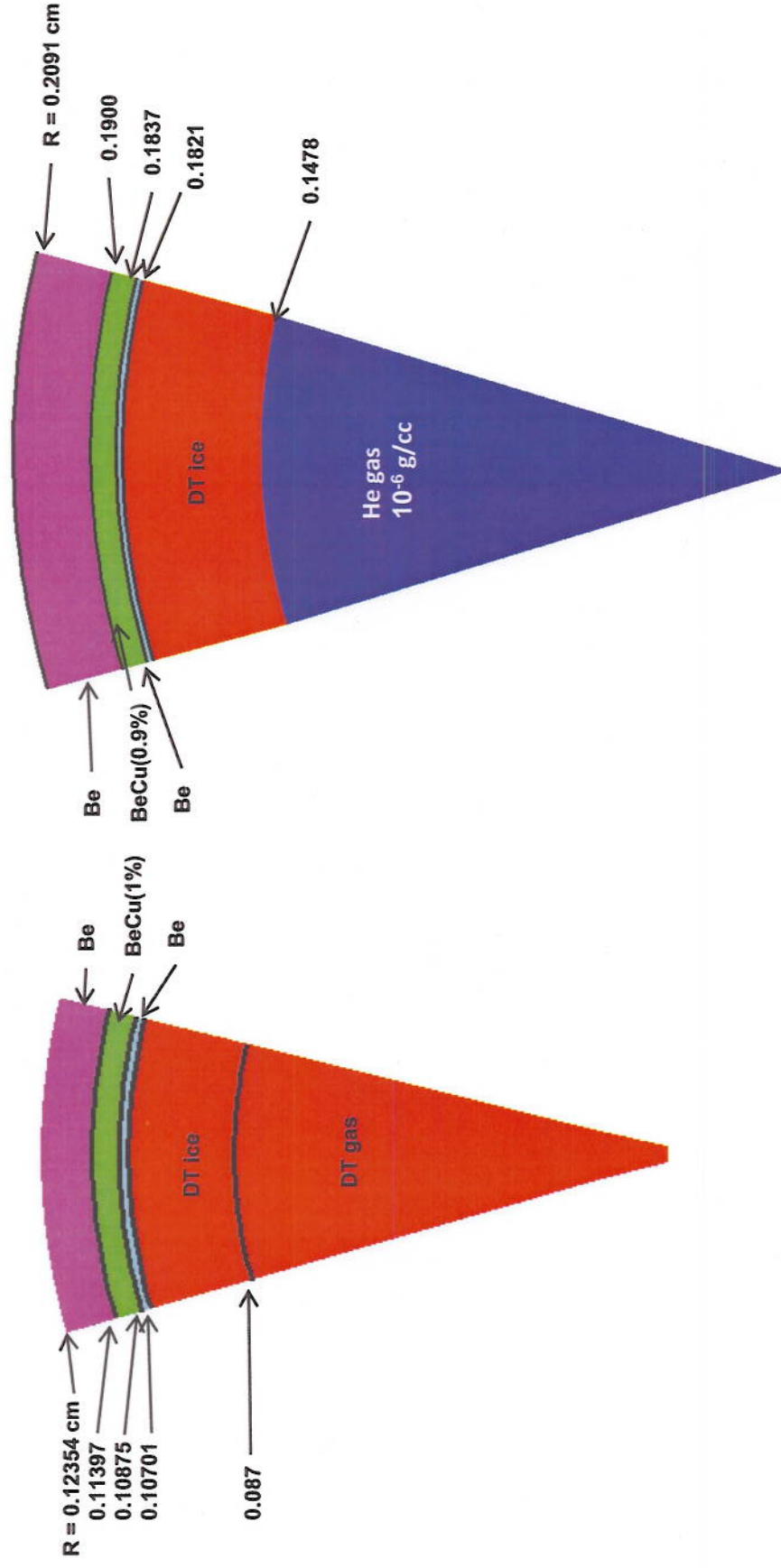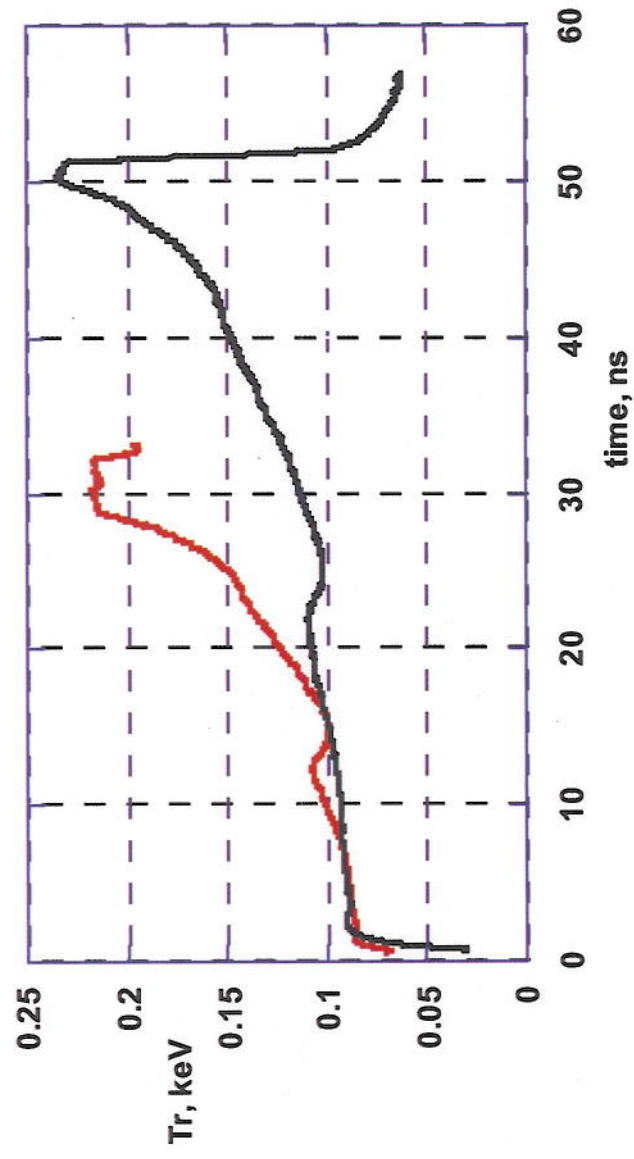
Figures for PoP article

Figures 1a & 1b

R = 0.2091 cm
0.1900
0.1837
0.1821
0.1478

DT ice

He gas
10⁻⁶ g/cc

Be
BeCu(0.9%)
Be

Figure 1b
Reactor scale capsule

Be
BeCu(1%)
Be

DT ice

DT gas

R = 0.12354 cm
0.11397
0.10875
0.10701

0.087

Figure 1a
NIF scale capsule

Figure 2

Figures 3a & 3b
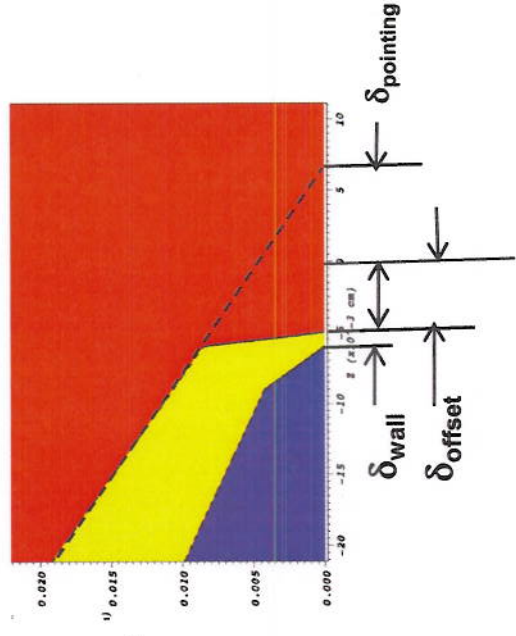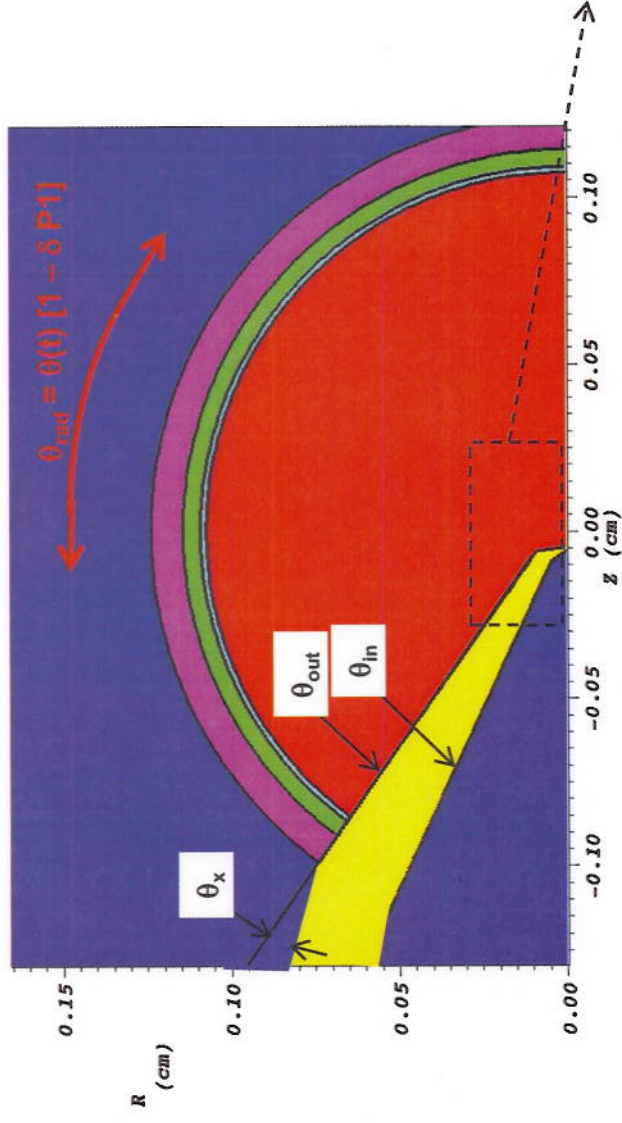
Figure 4
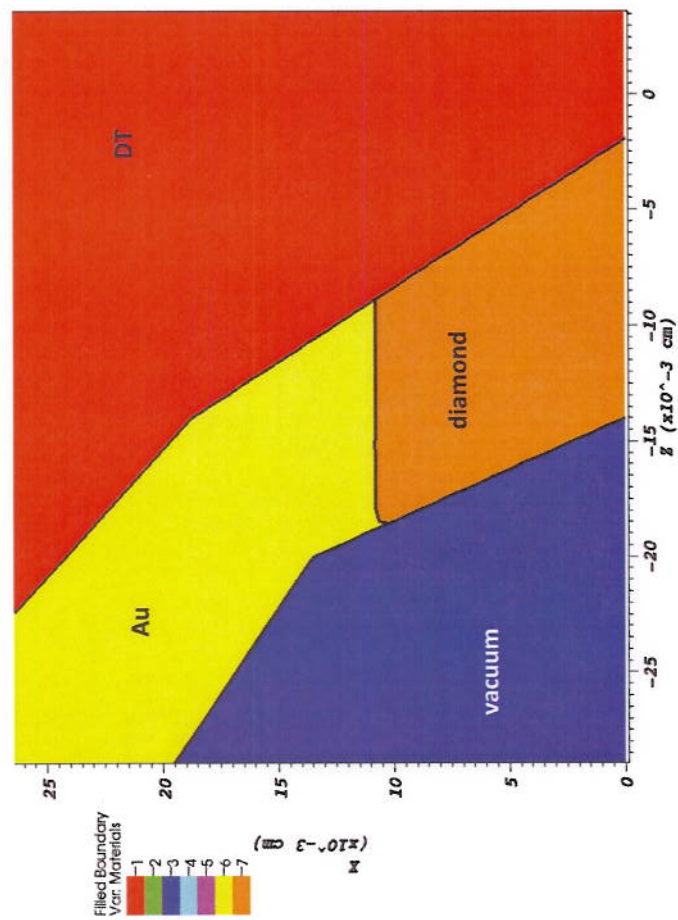
Figures 5a, 5b, and 5c

Figure 6

Surface for the FDS

Hohlraum gas

Ablated Be

Ablated gold from the cone

Pseudocolor
Var: trad
— 0.1132
— 0.08491
— 0.05661
— 0.02830
— 0.740e-07
Max: 0.1132
Min: 0.740e-07

Z

z (cm)

0.70 0.60 0.50 0.40 0.30 0.20 0.10

0.10 0.00 -0.10 -0.20 -0.30 -0.40 -0.50 -0.60 -0.70
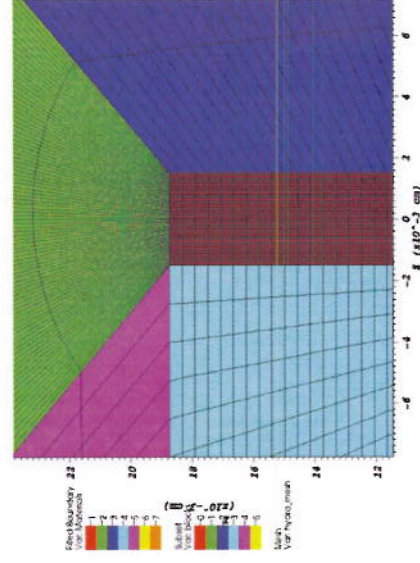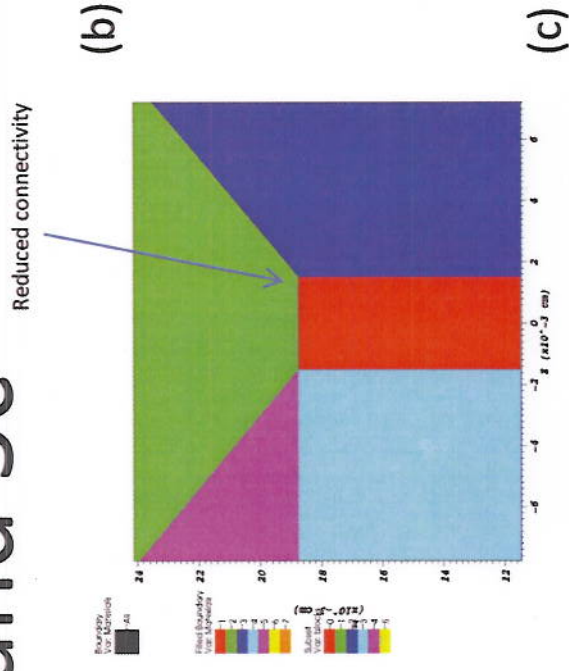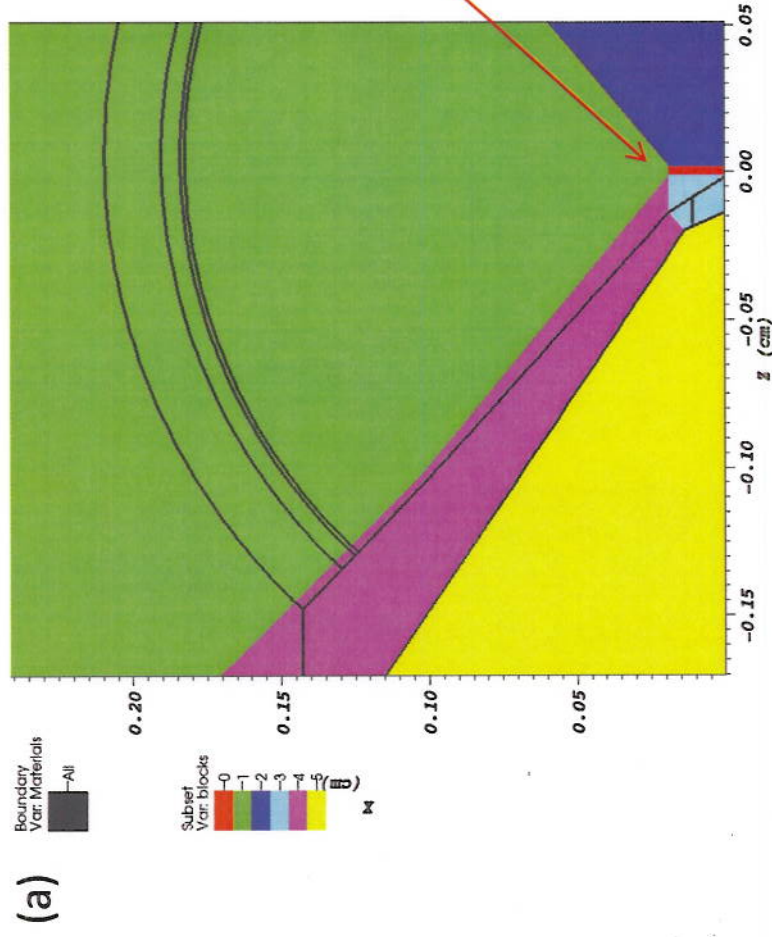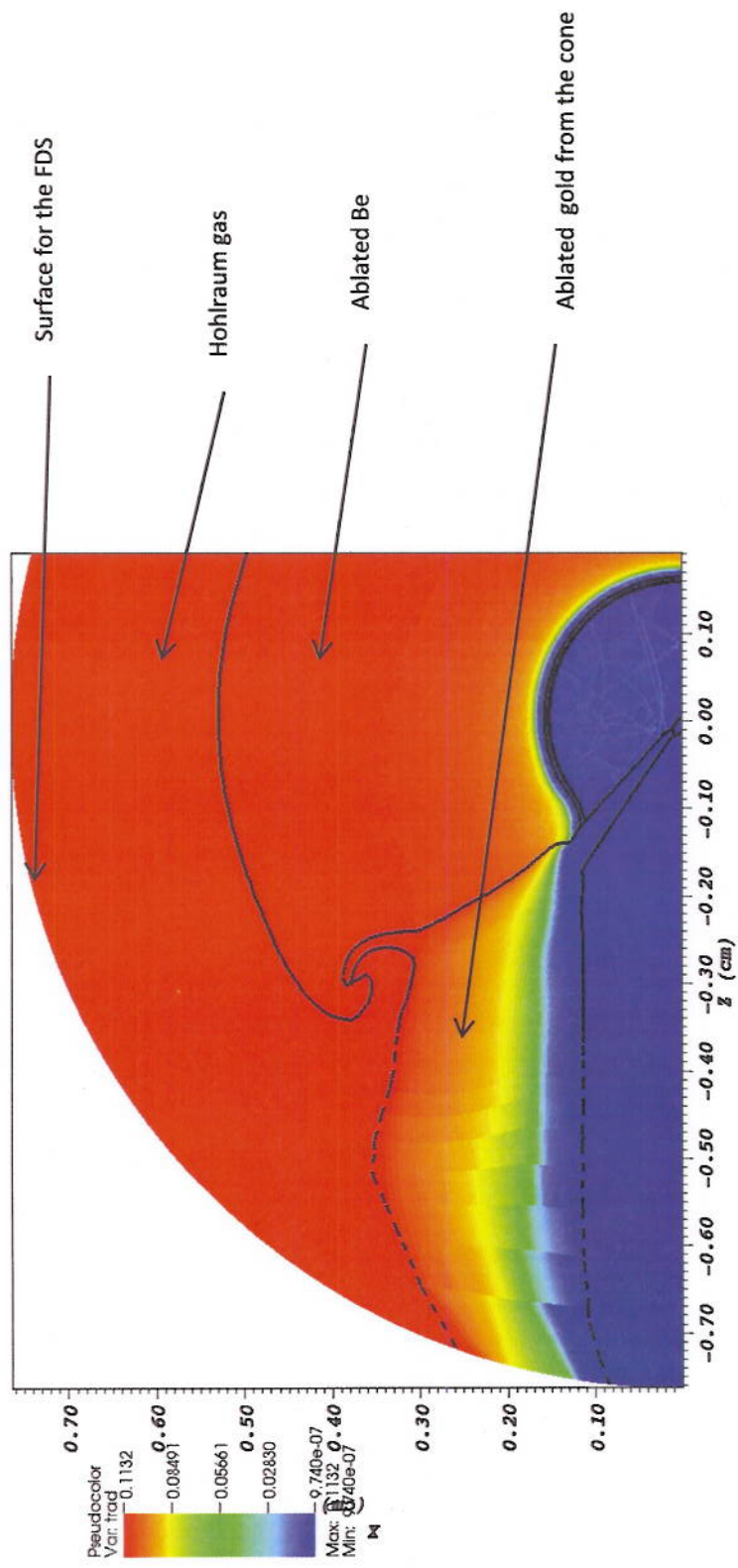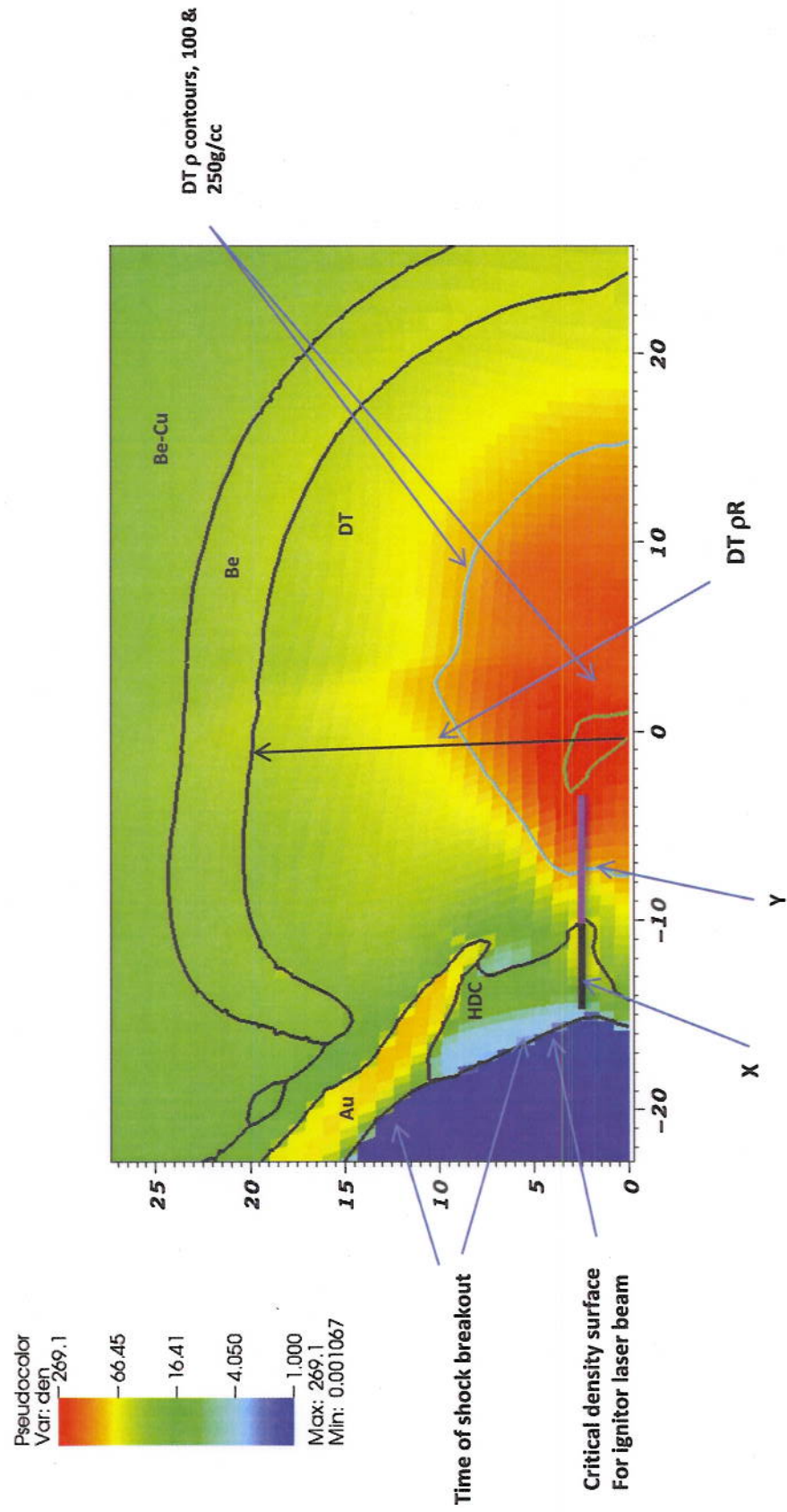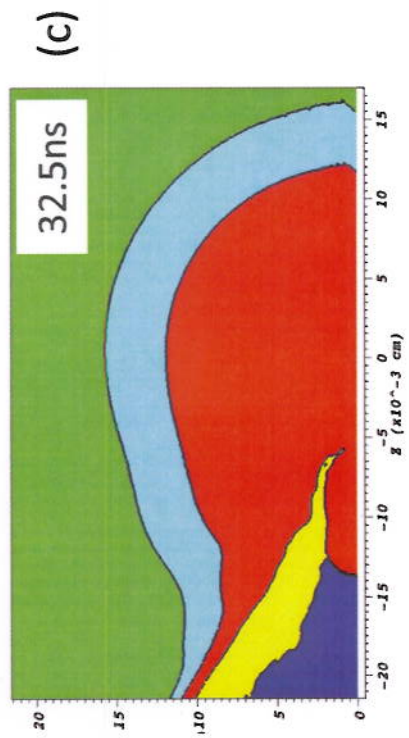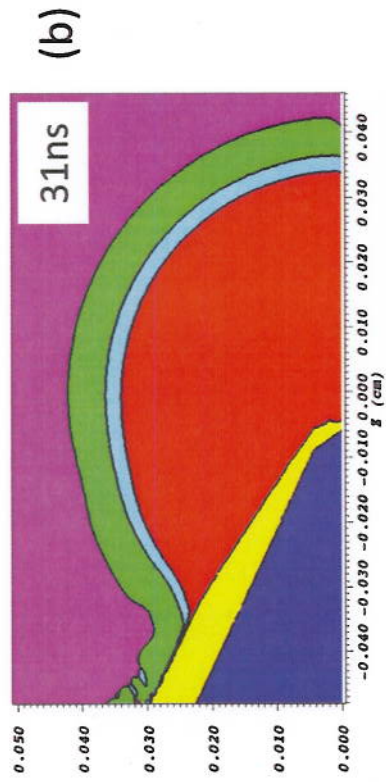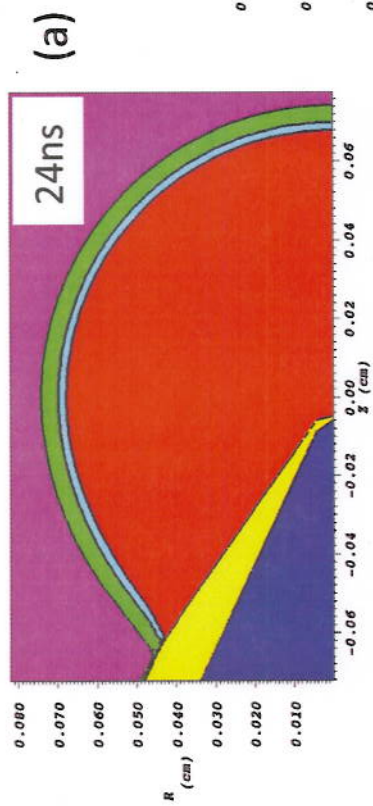
Figure 7

Figure 8

Figure 9
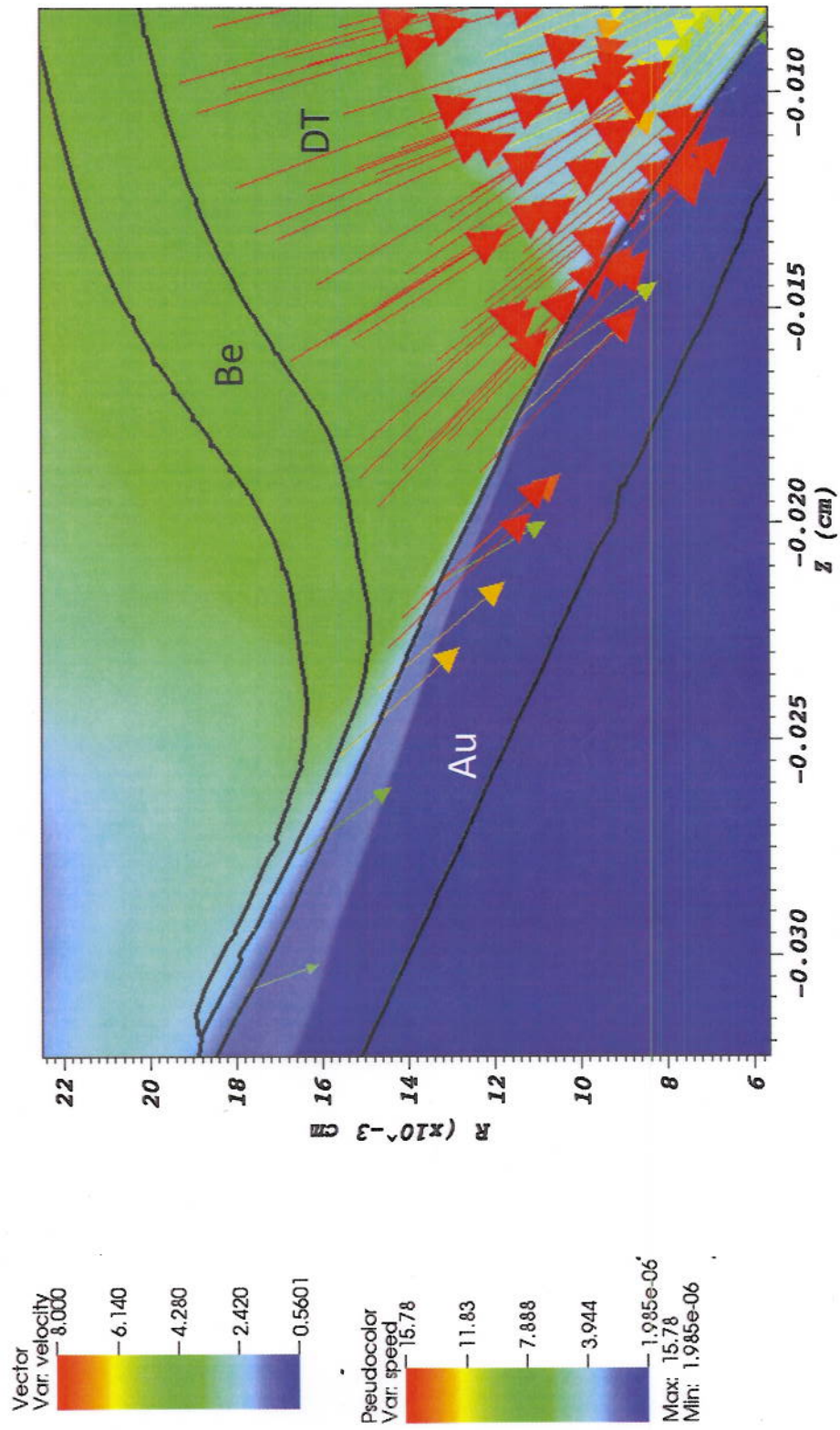
Table 1

Run	Tip of nose, μm	P1 offset, μm	CONE OFFSET, μm	X, μm	IX, g/cm²	Y, μm	IY, g/cm²
D2DZ	15	50	75	20-50	0.02-0.20	90	1.5
D2EA	15, sloped	50	75	15-40	.03-.09	115-125	1.6
D2EB	-20, sloped	50	75	10-30	.01-.05	120-140	1.53-1.61
D2EC	-20, sloped	50	0	25	0.08	120	~1.65
D2EF	100	50	75	120	1.3	40	0.7
D2EG	60	50	75	65	0.4	80	1.4
D2EH	60	0	75	50-150	0.15-1.43	30-90	0.7-1.5
D2EI	60	-50	75	50-220	0.035-2.28	19	0.41
D2EJ	60	25	75	29-110	0.12-0.66	64-102	1.1-1.5
D2EK	60; r=100	0	75	24-200	0.044-1.17	40	0.81

X   distance across HDC at time of peak DT ρ
IX   integral of ρ across X
Y   distance from tip of HDC to peak DT ρ at time of peak DT ρ
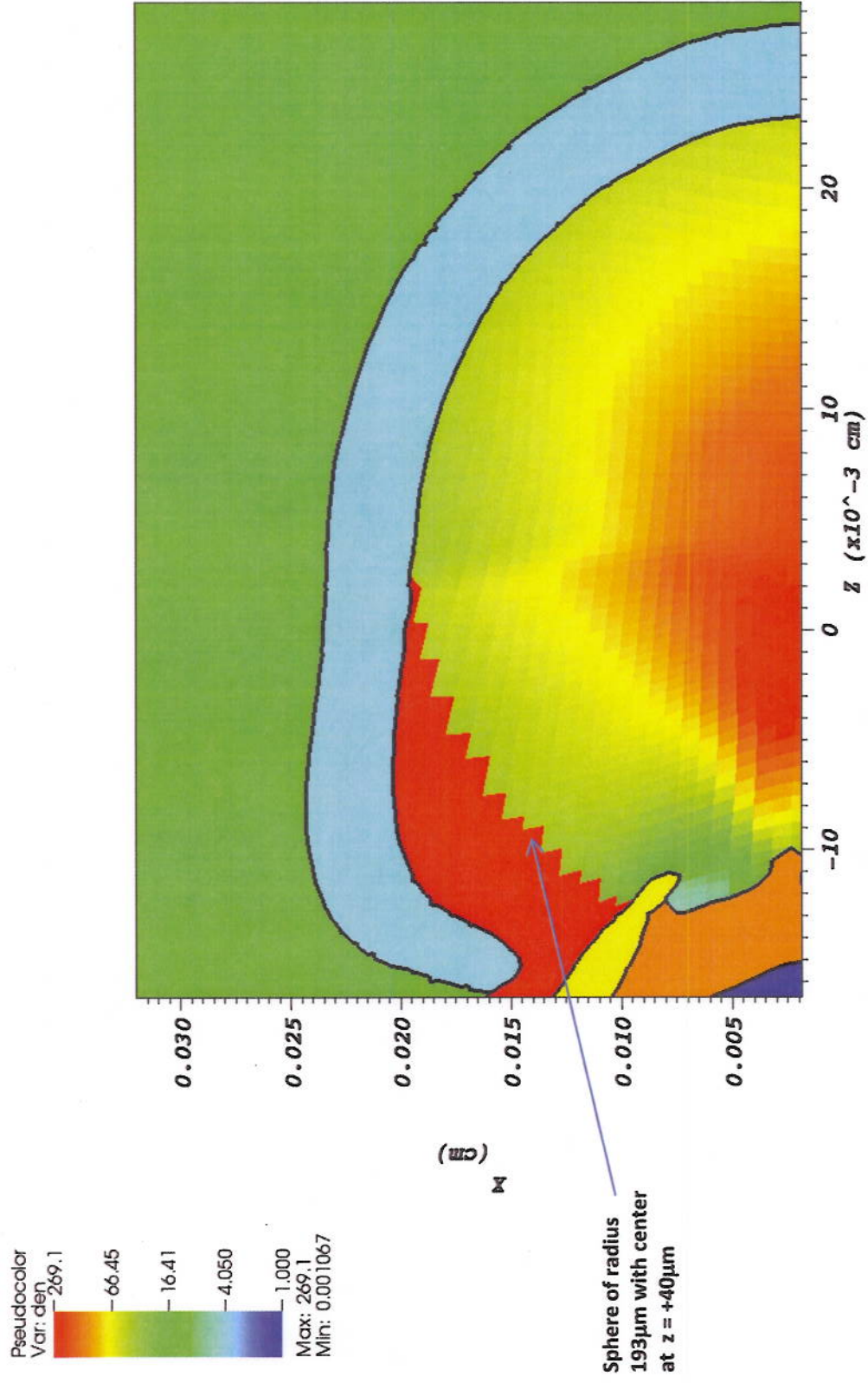IY   integral of ρ across Y
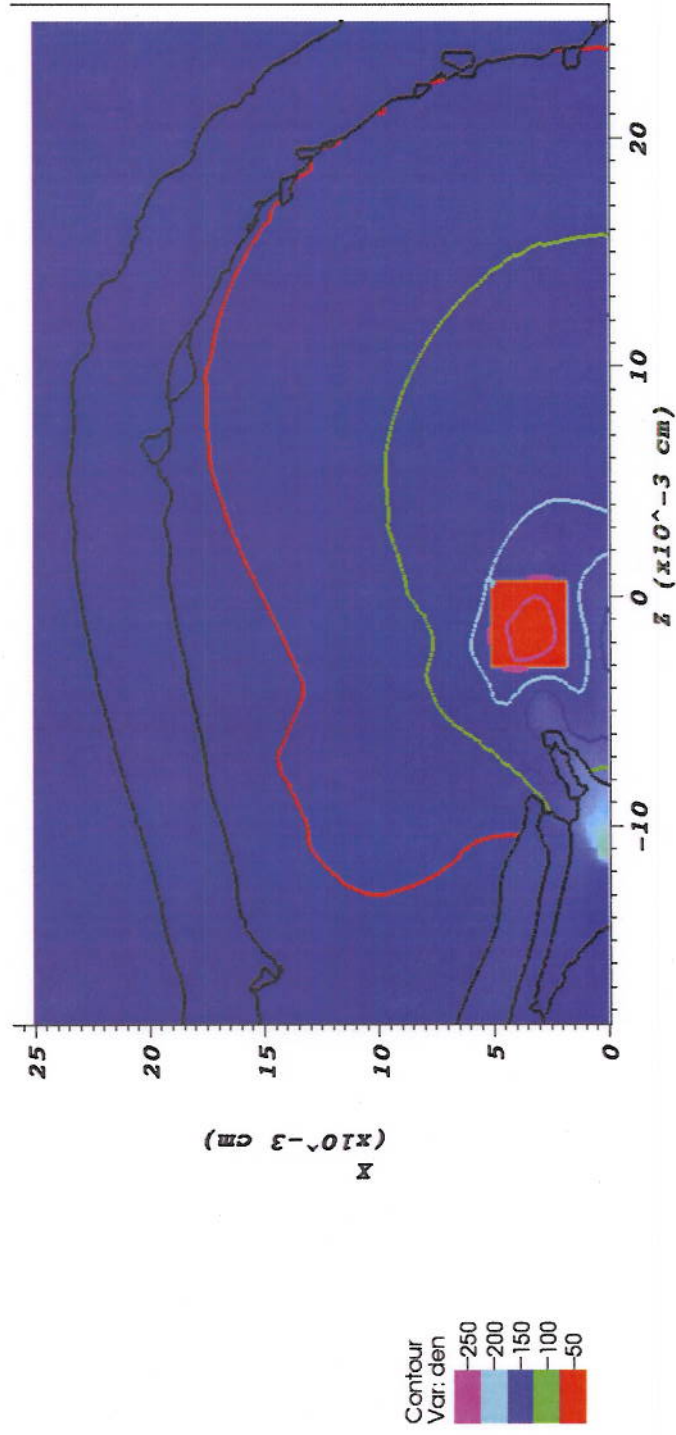
Figure 10

Figure 11

Figure 12